PROCEEDINGS, 45th Workshop on Geothermal Reservoir Engineering
Stanford University, Stanford, California, February 10-12, 2020
SGP-TR-216

Geophysical Observations and Integrated Conceptual Models of the San Emidio Geothermal Field, Nevada

Matthew Folsom[1], Ryan Libbey[1], Daniel Feucht[1], Ian Warren[2], Stefano Garanzini[3]

[1]Ormat Technologies, Inc., 6140 Plumas St, Reno NV 89503

[2]National Renewable Energy Laboratory

[3]CGG Multi-Physics Imaging, Milan, Italy

mfolsom@ormat.com

Keywords: Geophysics, magnetotellurics, gravity, geothermal exploration, integrated geologic model, passive micro-seismic, Pacific DC Intertie.

ABSTRACT

The San Emidio Desert hosts a hidden, forced-convection geothermal resource situated within a prominent right-step of the Lake Range in northwestern Nevada. The site has produced power since 1988, undergoing several phases of development since. Recent exploration drilling 1.5 to 2.5 km to the SW of the current production area has confirmed 162°C fluids 540 m below the surface with favorable permeability for development. This paper presents results from an integrated modeling study of the system that takes advantage of new geophysical data sets, including 211 broadband magnetotelluric stations, 1207 gravity stations, 176 line-km of ground magnetic data and a passive seismic experiment conducted with 1302 stations of 6 geophones each. These data are considered within the context of drilling results and other datasets to develop updated geologic and conceptual models of the geothermal system. Notable results are: (1) imaging of an extensive zone of mineralized/silicified Tertiary sediments along an outflow path and up-dip of normal faulting; (2) imaging of two distinct dome-shaped electrical conductors situated above zones of enhanced temperature and permeability; (3) coincidence of one of these zones with enhanced semblance of passive micro-seismic signals observed using a dense array; and (4) added constraints on the fault block geometry within the right step of the Lake Range, with implications for understanding the controls of deep permeability in the system.

1. INTRODUCTION

Situated along the western edge of the Lake Range, NV, the San Emidio geothermal resource area (Figures 1 and 2) hosts a classic Basin and Range style, forced convection geothermal system with ample surface alteration but no active thermal manifestations (note: there are reports from the 1990s of weak steam vents that once existed along the outflow path). Deep circulation of fluids is enabled here by fault-hosted permeability associated with dilation along a right step in normal faulting along the Lake Range (Rhodes et al., 2010; Rhodes, 2011, Teplow and Warren, 2015). A prominent characteristic of the field is a long (~5 km), shallow, range-parallel northward outflow path that lies up-dip of normal faulting (Matlick, 1995, Rhodes, 2011). First developed in 1987 and originally known as the Empire geothermal system, the resource has been expanded over time from an installed capacity of 3.6 to 14.7 MW. Current net generation is 11 MW. The field has been reconfigured several times as new wells were drilled, and the resource became better understood. Several rounds of geophysical data collection and modeling (Teplow et al., 2011; Eneva et al., 2011; Basler-Reeder 2015; Dierkhising 2015; Warren et al., 2018, Reinisch et al., 2019), and exploratory drilling (Teplow and Warren, 2015) have pushed the conceptual center of the field further south and southwest from its original position. In 2017, exploratory slim well 18-21 encountered 162°C fluids at a depth of 540 m with an estimated productivity index of 82 gpm/psi, making it the hottest and most permeable well in the field, and its most southern. The history of drilling successes and failures at San Emidio demonstrate that understanding the structure of the step-over fault system, most of which is buried under hundreds of meters of basin fill, is key to fully developing the resource. In this study, we have combined new geophysical surveys with publicly-funded datasets to develop an improved conceptual model of the system, with focus on the hidden step-over geometry from which it appears to emanate.

This study is composed of three main components: (1) we combined a new magnetotelluric (MT) dataset with existing data (Warren, 2018) and applied a modern 3D inversion routine (Mackie et al., 2001; Mackie and Watts, 2012; Soyer et al., 2018b) to image the 3D resistivity structure over the field and along its prominent outflow path; (2) we forward-modeled an extensive gravity dataset, cooperatively informed by geologic mapping (Rhodes et al., 2011), drilling data, MT and other results; and, (3) we constructed a 3D conceptual block model of the subsurface. Finally, we juxtapose our results with the passive seismic emission dataset presented in Warren et al. (2018). The results provide an interesting case study for interpreting resistivity models over Basin and Range hosted geothermal systems, which are not as prevalent in the literature as those over high-enthalpy, free-convection systems such as those found in Iceland, New Zealand, Indonesia and other volcanically active settings.

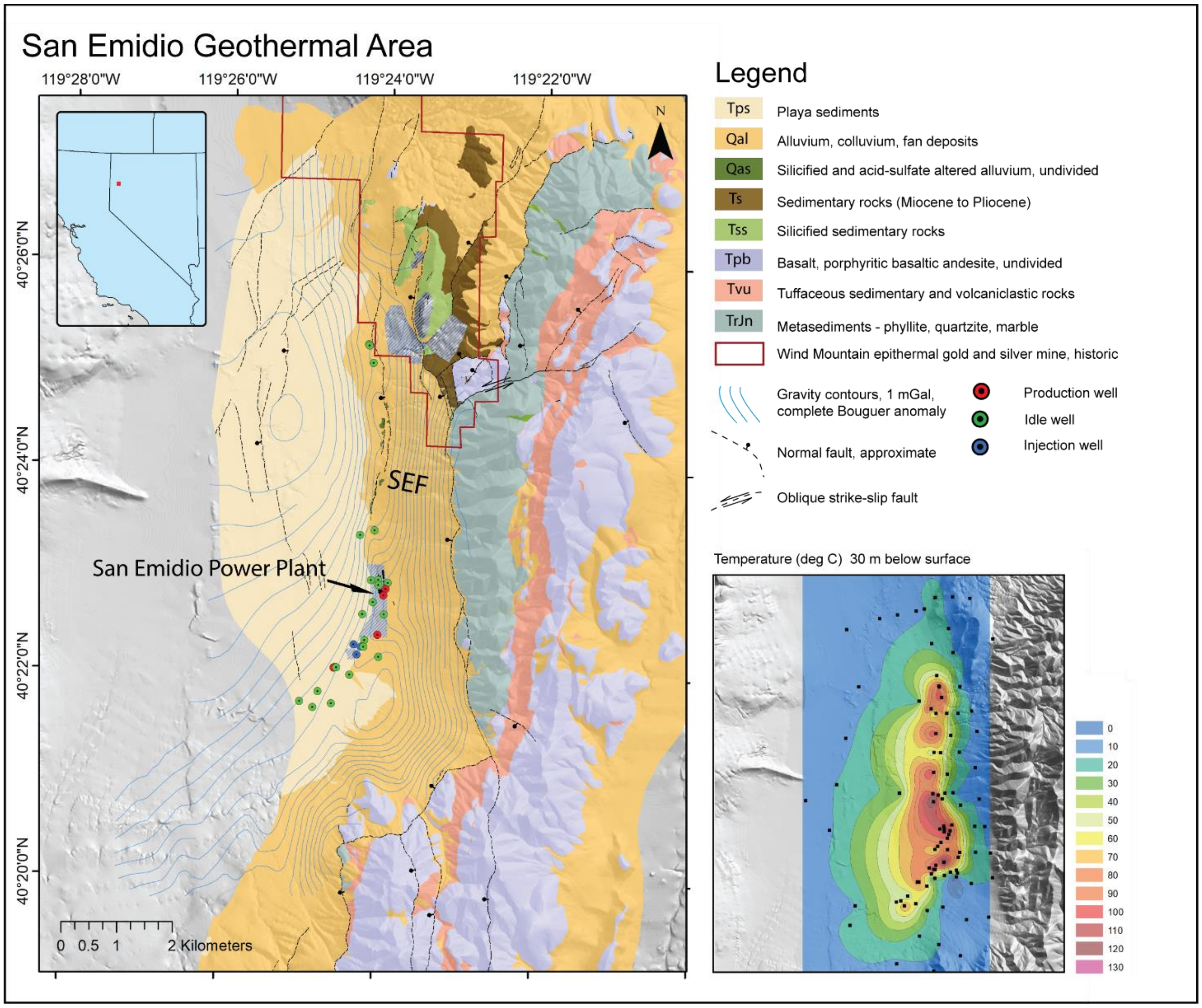

Figure 1: Overview map of the San Emidio Geothermal area and Wind Mountain epithermal gold mine. Geologic map simplified from Rhodes et al. (2011). Deeper wells shown in red, green and blue. SEF: San Emidio fault zone. Inset map: contoured shallow temperatures recorded 30 m below surface. Black squares represent TG well control.

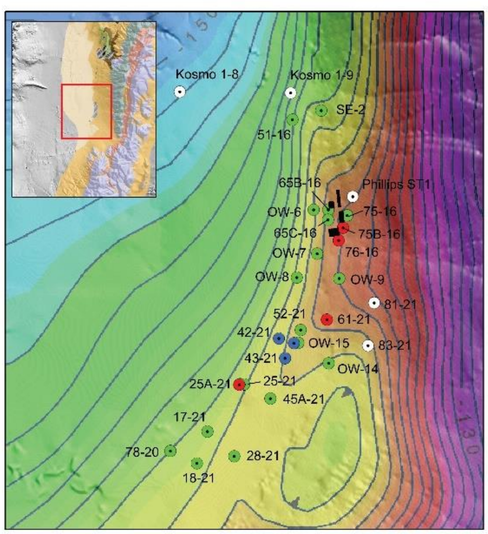

Figure 2: Detailed wellfield map on gravity complete Bouguer anomaly (1 mGal contour interval). Production wells are shown in red, injection wells in blue, idle wells in green, P&A'd wells in white.

2. GEOLOGIC SETTING

The geologic structure of the Lake Range and adjacent San Emidio Desert is controlled on a large scale by the interaction between two structural regimes: Basin and Range extension and northern Walker Lane dextral shear. The northwestern Basin and Range extensional regime accommodates approximately 3 mm/yr of mostly WNW extension in the study area (Hammond and Thatcher, 2005) and NNE-striking normal faulting. Many of the NNE-striking normal faults in the northern Basin and Range are locally linked by ENE-striking normal or oblique faults (Faulds et al., 2006). The Walker Lane transtensional belt, just south and west of the study area, accommodates 15 – 25% of the Pacific-North American plate motion (Faulds et al., 2005). Interaction between these two zones is complex, with dextral strike slip faults of the Walker Lane terminating into north striking, west dipping normal faults of the Basin and Range (Faulds et al., 2005, 2006; Drakos, 2007).

Locally, the northern Lake Range is composed of a system of east-dipping (~20°) fault blocks, faulted on their western sides by right-stepping, west-dipping en echelon normal faults (Drakos, 2007). The current power plant and many of the northern production wells are located near the southernmost expression of a Holocene piedmont scarp, known herein as the San Emidio Fault (Figure 1), which hosts zones of intense hydrothermal alteration. Near the San Emidio Geothermal site, range-front and range-parallel piedmont faults bound the Lake Range and make two prominent right steps. North of the plant, an older right step hosts a Miocene epithermal gold and silver deposit, and immediately south of the plant a larger right step hosts a dilated fault geometry that appears to control the locus of upflow for the modern San Emidio geothermal system (Rhodes et al., 2010; Faulds 2013). At the southern step-over, structures that accommodate strain between right-stepping normal fault strands are buried under several hundred meters of basin fill.

At the northern stepover, however, many of the accommodating structures are exposed. This location hosts the historic Wind Mountain gold and silver mine (Figure 1), a low-to-intermediate sulfidation, hot-spring style epithermal deposit (Ristorcelli and Dyer, 2012). The main range front fault splinters here into an ENE striking sinistral oblique-slip fault (Rhodes et al., 2010), and several closely-spaced normal faults that continue northward where they intersect with NNE-striking, west dipping normal faults. This step-over system exhibits elements of a relay structure, with an accommodation zone connecting sub-parallel fault segments (e.g. Fossen and Rotevatn, 2016). Such structures have been associated with elevated fluid-flow in both ore-mineralization (Cox, 2005) and geothermal settings (Faulds et al., 2011, 2013).

The Northern Lake Range is overlain by Tertiary volcanic and sedimentary units that rest unconformably on Mesozoic metamorphic basement. Tertiary basaltic andesites are locally thick (500 m or more) and crown the highest points of the Lake Range (Rhodes et al., 2011). Underlying this is a more complex unit of Tertiary sedimentary and volcaniclastic units with three thinner lenses of intermediate lava flows. The basement is Triassic-Jurassic metasedimentary rocks assigned to the Nightingale Formation (Bonham and Papke, 1969; Moore, 1979). Exposed near the Wind Mountain mine are upper Miocene sedimentary units and lacustrine deposits with minor intermediate lava flows (Moore, 1979) which have been locally altered and silica flooded (Rhodes, 2011). Alteration found along the San Emidio fault scarp is younger and Quaternary in age. A long (~5 km) rectilinear zone of acid-sulfate alteration follows the scarp forming various alteration products (Matlick, 1995; Rhodes, 2011) including native sulfur and mercury sulfides, massive siliceous sinter, silicified sands and silicified lacustrine deposits.

3. HISTORY OF THE FIELD

Early exploration began in the late 1970s with several geothermal companies conducting surveys and drilling in the study area. Perhaps the most significant finding at this time resulted from the drilling of 63 temperature gradient (TG) wells, which defined a shallow, ~134 °C, range-front parallel outflow reservoir over the San Emidio fault zone (Matlick 1995). This temperature data along with modern additions is contoured at 30 m depth in Figure 1 (inset). Figure 2 shows a detailed view of the wellfield configuration. In 1976, Phillips drilled ST-1, a deep temperature observation well to 590 m which struck an interpreted fault zone and encountered a maximum temperature of 148°C. Chevron subsequently drilled two of the deepest wells in the field, Kosmo 1-8 and 1-9 to 1223 m and 1616 m, respectively. These attempts to find the source of the shallow outflow were unsuccessful. Both passed through a shallow temperature roll-over, became cooler at depth and lacked permeability.

In the mid to late 1980’s development for the original Empire power plant included the drilling of more than a dozen wells in an area about 1.5 km SSW of the current facility, mostly targeting the shallow geothermal aquifer. None of these discovered a deeper resource. In 1987, AMOR II Corp. commissioned a 3.6 MW binary power plant that utilized these wells. In the early 1990’s, Empire Farms established a vegetable dehydration project at the location of the current power plant and drilled nine wells to support operations. 65C-16 was completed to 160 m, producing 131°C fluid with minimal drawdown and became their primary production well. In 1994, well 75-16 was deepened from 330 m to 555 m and discovered fracture permeability. This well produced 152°C with no measurable pressure drawdown (Matlick, 1995). After dozens of wells drilled, this was the first to encounter successfully permeability and temperature from the deeper reservoir.

U.S Geothermal acquired the project in 2008 and began efforts to maximize the wellfield. In 2012 a new 14.7 MW capacity plant was commissioned near the location of the vacant dehydration plant. U.S Geothermal applied for and received a DOE funded cost share grant to further explore the project (Teplow et al., 2011; Teplow and Warren, 2015). This project collected a new set of geophysical data (gravity, ground magnetics, PSInSAR and several seismic reflection/refraction lines) and ultimately concluded with drilling exploration wells OW-6, 8, 9, 12, 14, 15, 61-21 and 45A-21. These efforts demonstrated that a hotter, deeper resource was located to the SW of current production. The southernmost of these, 45A-21, encountered the highest temperatures yet recorded in the field of 161°C near 670 m depth but cooled to 154°C at 971 m where it was completed in the Nightingale Formation. The well encountered no significant permeability. Three injection wells, with depths of 100-250 m (cased to 25-76 m) accept all of the fluid from the plant with no wellhead pressure. These wells were drilled between 1986 and 1988 as a part of the original Empire geothermal power plant.

U.S. Geothermal continued exploration in the southern field with another deep TG drilling campaign in 2015. They later deepened five of these, three of which became the most promising wells in the field: 25-21, 17-21 and 18-21. Each of these wells encountered commercial temperatures and permeability. The southernmost of these, 18-21, was the hottest and was evaluated with a productivity index of 82 gpm/psi at 162°C. Permeability in nearby wells 78-20 and 28-21 were an order of magnitude less than 18-21 and 17-21, confining the zone of interest to a narrower, SSW trending feature. U.S. Geothermal was acquired by Ormat Technologies in 2018, who then twinned 25-21 with 25A-21 in October of that year. During an initial production test, 25A-21 produced 161°C brine with a productivity index of 105 gpm/psi. An Ormat line-shaft pump has been installed and the well has a proven (pump-limited) production capacity of 4000+ gpm.

4. DATA AND METHODS

4.1 Magnetotellurics

Magnetotellurics is a passive imaging technique that uses small amplitude, naturally occurring electromagnetic (EM) waves to extract information about the electrical resistivity structure of the subsurface (Cagniard 1953). Global lightning events and solar wind interactions with the Earth's magnetosphere are the source of this energy. Naturally occurring EM waves are mostly reflected upon incidence with the Earth due to a sharp resistivity contrast with air, however, a small portion of the energy diffuses into the ground (Jiracek et al., 1995) at near-vertical incidence angles caused by the high index of refraction at the surface. This verticality is a crucial assumption, as incident waves are assumed to be planar (oscillate only in the X-Y plane). At MT recording locations, temporal variations in natural electric and magnetic fields are recorded as perpendicular vector components. Time series recordings of these vector components are windowed and transformed into the frequency domain, allowing for the estimation of an impedance, Z, from the ratio of the electric (E) and magnetic (H) field spectra:

$$\boldsymbol{E} = \boldsymbol{ZH} \tag{1}$$

Where **Z** is a complex 2x2 tensor at each investigated frequency. Complexity of structure necessitates a tensor form of **Z**. **E** and **H** represent the measured electric and magnetic field components in the frequency domain. Once the components of **Z** are estimated, they are commonly displayed as apparent resistivity and phase with period (or frequency) along the x-axis, which is a proxy for depth of investigation.

4.1.1 MT Data

Two MT datasets are described in this report (Figure 3) and were combined for use in a final 3D inverse model. The first was collected in 2016 and 2017 by Quantec Geosciences, as part of a DOE-funded project (Warren et al., 2018). The Quantec data can further be divided into two different survey geometries: Standard MT sites, where north (E_x) and east (E_y) directed dipoles, each 200 m in length, are laid out in an L-configuration. A second, more closely-spaced survey used a profile configuration, where each recording site has a single E_y dipole but two E_x dipoles along an E-W profile direction. Profile sites are processed with each set of E_x field data separately, resulting in two adjacent soundings per recording site. These geometries are referred to in this report as Quantec MT and Quantec profile sites, respectively. All Quantec MT data employed porous pot non-polarizable electrodes and Phoenix MTC50 or MTC80 magnetic field sensors. Both data types cover a range from 250 Hz – 1000 s (Figure 3). Each site also recorded vertical magnetic field data, allowing for the estimation of induction vectors (or tipper). A designated remote reference station was located 40 km to the south in an adjacent basin. Transfer functions were generated using the robust processing code of Egbert (1997).

This public MT dataset was unfortunately plagued by near-field noise from the Pacific DC Intertie (PDCI), a 500 kV direct current power line that passes through the study area (Figure 3). The term "near-field" implies that this energy does not satisfy a plane wave description and therefore violates the MT assumptions. The PDCI was shut down for maintenance when the survey began, but became energized about six days into data collection, impacting 90 of 120 soundings recorded. This power line is notoriously detrimental to MT data, especially in the range of 3 – 0.1 Hz. The effect is not easily remedied by remote-reference processing unless the remote is 60 km or more from the noise source (Wannamaker et al., 2005). The noise it creates is broadband in nature and cannot be removed via a notch filter such as that from the 60 Hz power grid. Figure 3 shows the results from affected Quantec stations 16A and 12A. The red box denotes the band most impacted by this near-field noise source. Its impact on the data is a steep increase in apparent resistivity (with a slope approaching 45 degrees on a log-log plot) with a corresponding steep decline in phase. At a certain longer period, the natural MT signals dominate over the near-field noise and the apparent resistivity curve exhibits a pronounced discontinuity. It is presumed that the curve is governed by the natural Earth response at longer periods beyond the discontinuity. For the MT data at San Emidio, the XY mode, which has a north-south oriented dipole, is more impacted than the YX mode, but both are suspect. This band must be carefully edited prior to modeling to avoid generating spurious artifacts. Greyed-out points in Figure 3 were removed from the data prior to modeling. Solid red and blue lines show the fit of the synthetic Rho+ model (Parker and Booker, 1996), which is used as a general quality assessment of MT data. The Rho+ model tests the consistency between apparent resistivity and phase and assumes a one-dimensional resistivity structure. MT data that fit the Rho+ model are interpreted to have minimal effects from complex structures and/or near-field noise.

Conducting MT surveys near the PDCI warrants careful planning. The line runs from near the border of Oregon and Washington to Sylmar, CA and is operated by the Bonneville Power Authority (BPA). It transfers up to 3200 MW of hydroelectric power, and typically has periods of downtime for maintenance in the fall. In 2019, the line was completely down from October 13th – November 15th, followed by a period of intermittent testing between November 15th and December 7th (Kevin Wingert, BPA, personal communication, 2019). However, this schedule differs from year to year and should be verified before mobilizing an MT crew.

A second MT survey was commissioned by Ormat to investigate the regional context of the geothermal resource, including the step-over structure and the northern outflow path (Figure 3, black triangles). This survey was collected in October 2019 and timed to coincide with the scheduled maintenance of the PDCI. Data were collected by Zonge International using Zen receivers, porous pot non-polarizable electrodes, and Zonge ANT-4 magnetometer coils. The survey deployed 100 m dipoles in an L-configuration and vertical magnetic data were recorded to allow estimation of tipper. A designated remote reference station was maintained 50 km NNW of the study area on the edge of the Black Rock Desert. Data were processed using a proprietary Zonge code similar to Sutarno and Vozoff (1991) and Egbert (1997). MT transfer functions (impedance and tipper) were estimated for each site over a period range of 10^{-3} to 10^{3} s.

Other than the frequency band in the Quantec soundings that was impacted by the PDCI, data quality is generally high. The majority of the Quantec data were edited heavily between 0.3 and 20 s to reduce the impact of the power line noise. Another notable gap in the Quantec data is present at high frequencies (>250 Hz) due to the equipment configuration and sampling rates chosen. A select few sites from the Zonge survey exhibit pronounced distortion at high frequencies. The distortion manifests as frequency-independent static offsets of the XY and YX modes of the apparent resistivity curves, in some cases exceeding 80% of a decade when plotted on a log-log scale. Stations that appear to be distorted are generally confined to the northern region of the study area and located adjacent to the outflow path. These static shifts are not easily explained by topography or survey error, so we infer that they are instead caused by near-surface inhomogeneity in the resistivity structure (Jiracek, 1990; Pellerin and Hohmann, 1990). This seems plausible given the proximity of these stations to heavily altered outflow. Static distortions can contain useful information when modeled in 3D (Soyer et al., 2018), and we chose not to correct for them but rather to include them in the modeling strategy.

To visualize the data characteristics over the entire study area, parameter maps showing phase tensor ellipses (Caldwell et al., 2004) were produced to illustrate structural trends (Figure 4, left panels). Phase tensors are a principle component representation of the impedance phase tensor: flattening represents a split in the principle phase components and indicates the preferred direction of current flow, or the geo-electric strike. A 90-degree ambiguity exists, however. Over perfectly layered 1D structure, they become circular. Here we have colored the ellipses by the geometric mean of the principle phase tensor elements. Warm colors denote high phase, and a vertical transition from high to low resistivity This is a simplification meant for visualization purposes; it is valid only for 1D structure. Figure 4 shows the phase tensors from recorded data at 1 s and 10 s in the left panels. Missing ellipses in the Quantec survey show the extent of heavy data masking due to the PDCI. Overall, the ellipses vary smoothly from one to another in shape and color attributing to the high quality of the data that remains. Over the basin they begin to flatten at longer periods as they become sensitive to the underlying basement.

We also show the real part of induction arrows in the Parkinson convention (1983), which point toward conductors. Figure 5 (left panels) show the vectors from recorded data at 1 s and 10 s. The vertical magnetic component was strongly impacted by the PDCI and are similarly masked. At 1 s, the arrows point at infield heterogeneity such as the north-trending outflow zone and to an area within the Quantec profile sites. At 10 s they begin to align and uniformly point toward the thick package of conductive basin fill to the west. Both induction vectors and phase tensor ellipses have an added advantage of being insensitive to static distortions.

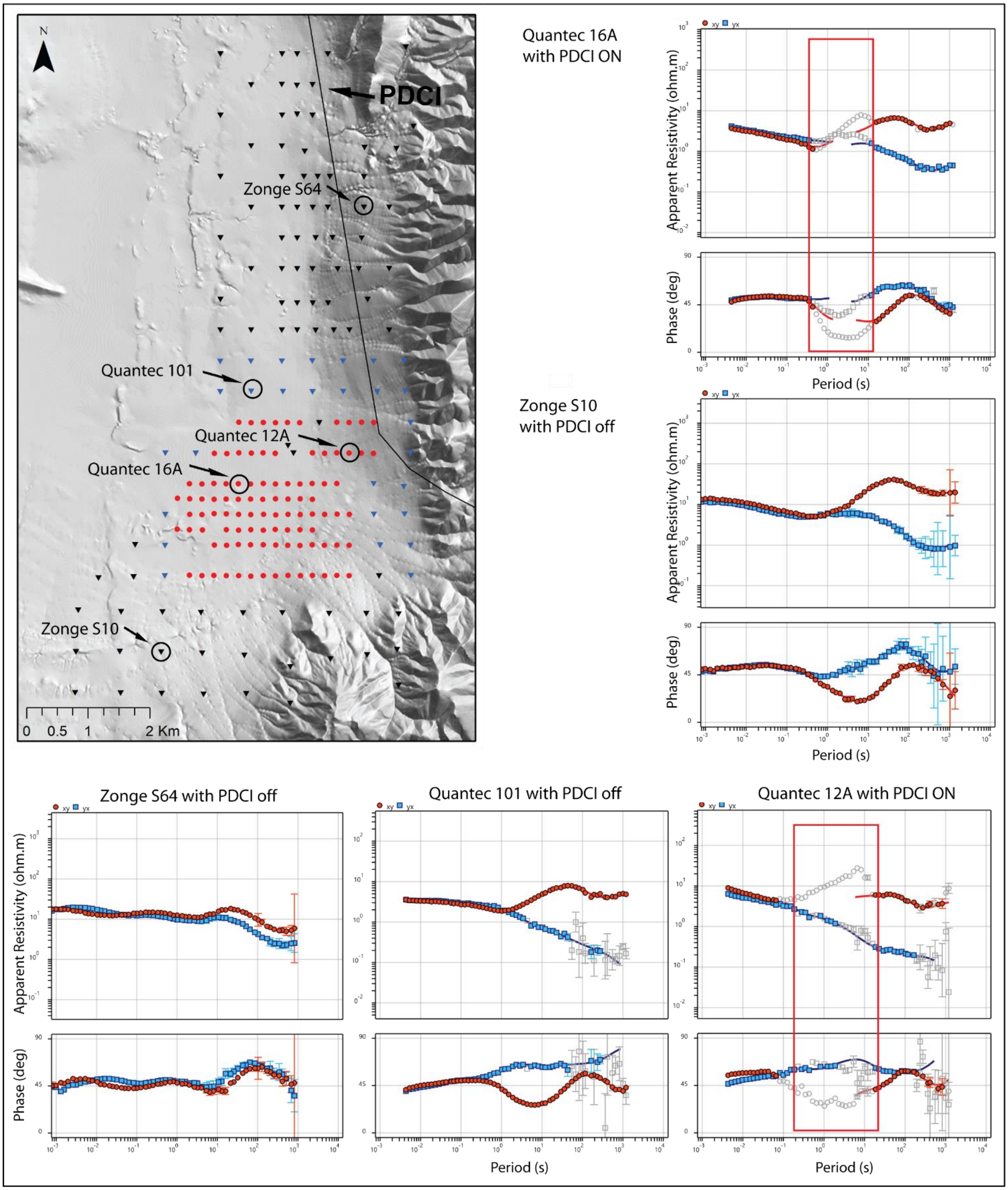

Figure 3: Map of recorded MT stations by their respective operators. Red circles: Quantec profile, blue triangles: Quantec MT, black triangles: Zonge broadband MT stations. Sample data are shown on top of Rho+ synthetic models (Parker and Booker, 1996). Masked points not used in modeling are greyed out. Red rectangles show the data band impacted by the PDCI.

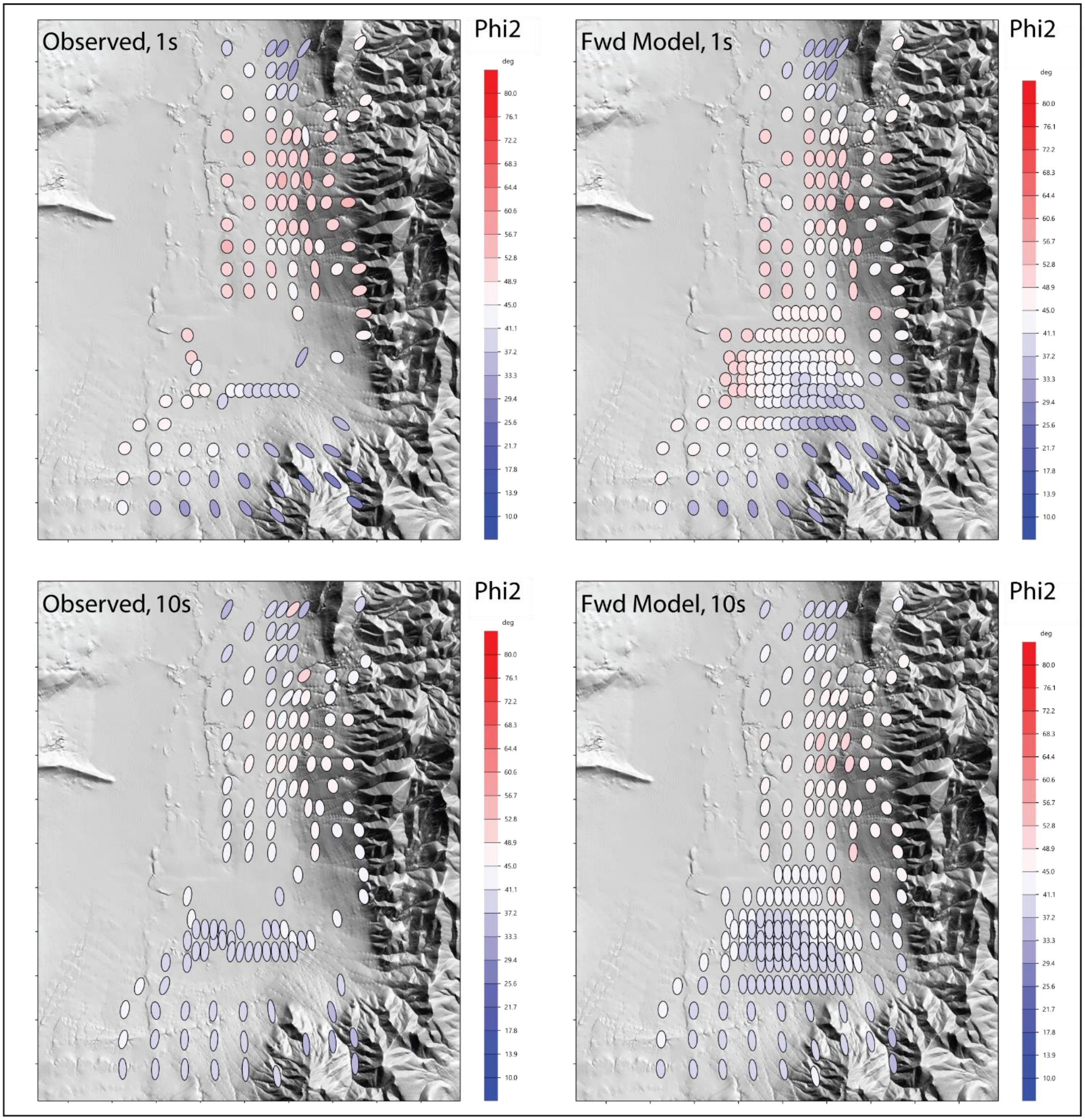

Figure 4: Phase tensors for both recorded data and forward model response from the final 3D MT inversion. Ellipses are colored by Phi2, or the geometric mean of the principle phase tensor elements. Warm colors denote a decrease in resistivity with depth, and cold colors an increase in resistivity with depth. Missing ellipses in observed data are caused by extensive masking of data in these bands.

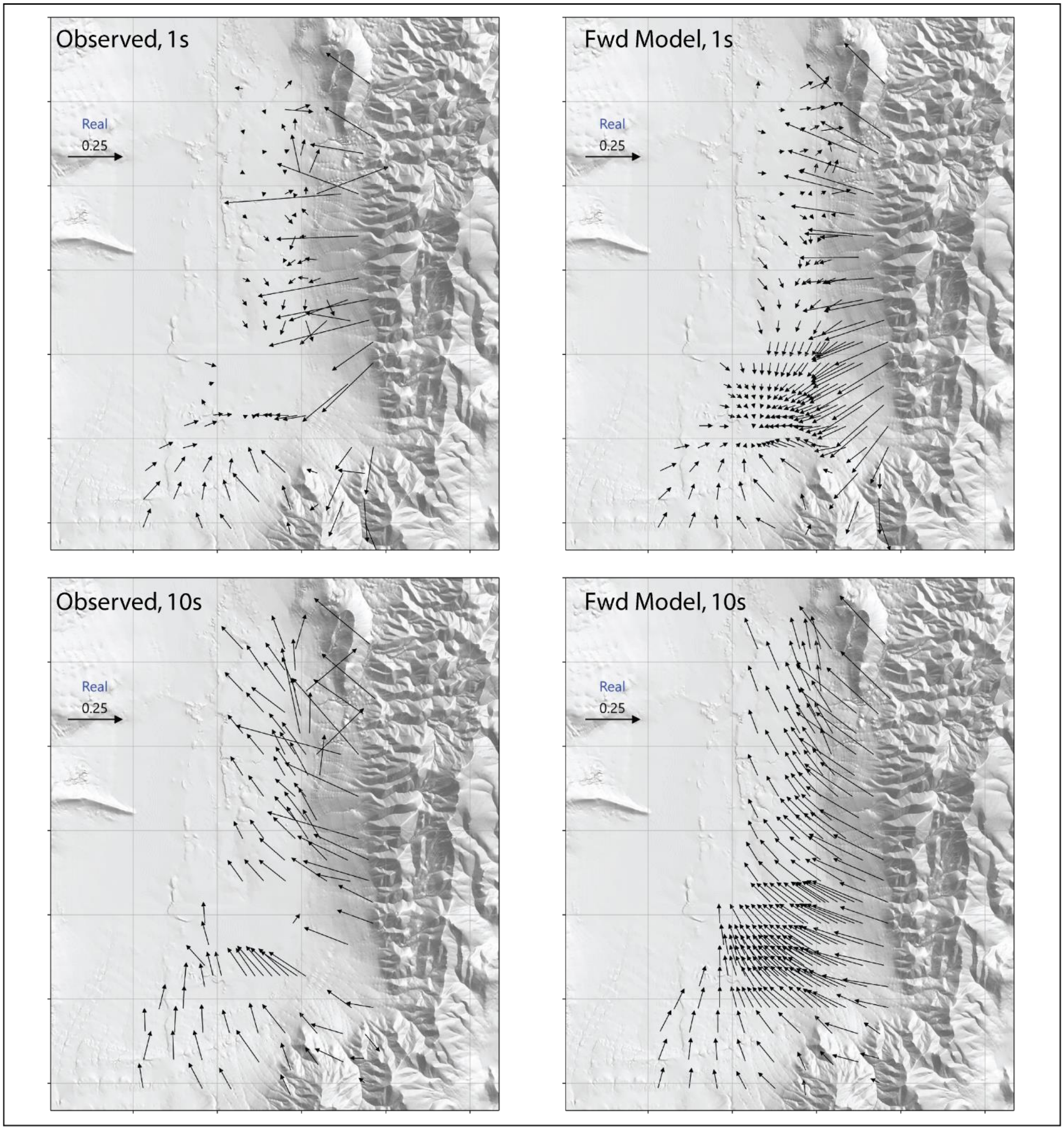

Figure 5: Induction arrows (real part) of both recorded data and forward model response of the first MT model, used as a starting model to the final MT inversion. The Parkinson convention (1983) is used where arrows point towards conductive features.

4.1.2 MT Methods and Model Generation

We modeled the combined datasets of 120 Quantec and 91 Zonge MT stations using CGG's proprietary RLM-3D inversion code. Parameter regularization follows a minimum-structure Tikhonov approach (Tikhonov and Arsenin, 1977), where an objective function that contains a regularization (smoothing) term is minimized using the method of non-linear conjugate gradients as described in Rodi and Mackie (2001). A grid was constructed with a fine inner core of 50 m x 50 m around the Quantec profile sites and 100 m x 100 m grid over the remainder of the survey. Topography was discretized at 10 m, resulting in a total of 2.8 million cells. To reduce processing times, data were subsampled to 5 frequencies per decade. Error floors were 5% for **Z** components and 0.02 for tipper were applied in the inversion settings.

Minimum structure models require a balance between producing the level of detail desired and suppressing artefacts. We took a phased-approach of running multiple inversions, with each run using the former as a starting model but with lower smoothing constraints. The first inversion began on a 20 ohm-m starting model, inverting for the full-tensor components of **Z** and tipper data. This model ran for 30 iterations, with different smoothness settings in the vertical (0.01) and horizontal (1.0) directions. A second and final inversion used only the components of **Z** and ran for an additional 30 iterations with reduced vertical (0.001) and horizontal (0.3) regularization. A depth-dependent weighting function was additionally applied to the vertical smoothness term, where the shallowest layers are multiplied by 0.1, increasing linearly to 1.0 at 500 m depth. The data fit rms value of the second and final model was around 1.

Earlier trials with this dataset included tipper values in the final model run, however, it had the effect of amplifying the north-going conductor near the PDCI to ~ 0.4 ohm-m (Figure 6, top left). To soften these effects, we removed the tipper data from the final model run. It is possible that the PDCI generates elevated vertical magnetic fields nearby even while turned off, given its size.

To address severe static distortion issues at some sites along the outflow, we inverted directly for distortion matrices at each site using the method described by Soyer et al. (2018). This weighted method, inherently linked to the smoothing constraint, allows for a real 2x2 matrix to be applied to each impedance tensor such that $\mathbf{Z}_d = \mathbf{CZ}$. The distortion matrix can transform **Z** to better fit the static shift; it is a useful tool but if over-weighted it can remove important features.

Constant-elevation slices through the final model are shown in Figure 6. A strong conductor is present at shallow depths under the PDCI, however, this conductive zone lines up well with anomalies in the gravity dataset just range-ward of the San Emidio fault zone. Recent shallow auger holes drilled in this zone indicate silt-rich lacustrine deposits. These units may also be clay-altered at depth due to advanced argillic alteration. It is possible that the magnitude of this conductor is overexaggerated because of the PDCI. Deeper in the volume, and best seen at 800 m elevation (Figure 6, lower left) the conductive trend changes strike to the SSW, hinting at the geometry of the step-over. Some trends near the Quantec profile sites (red circles) are suspicious in that they follow the survey geometry. A deeper, near perfectly E-W conductive feature in the northern part of the Quantec profile sites (Figure 6, lower right) may be the result of data gaps in the Quantec data, the physical distance between parallel lines of stations here, un-masked data that was influenced by the PDCI, or some combination of these. Drill data from well 25A-21 that falls in this zone does not agree well with the MT model; however, the model fits drilling observations very well in the southern (near 18-21) and northern (near 75-16) production zones.

To assess the data fit of the model, phase tensor ellipses and induction arrows calculated from the forward response to the 3D model are shown in Figures 4 and 5 (right panels). Forward-response phase tensors are calculated from the final model response, and forward response induction arrows are calculated from the first model that included tipper data in the inversion. These parameter plots match those from the data rather well but are considerably smoother. Induction arrows at 1 s point inwards to a portion of the field near the southern exploration wells.

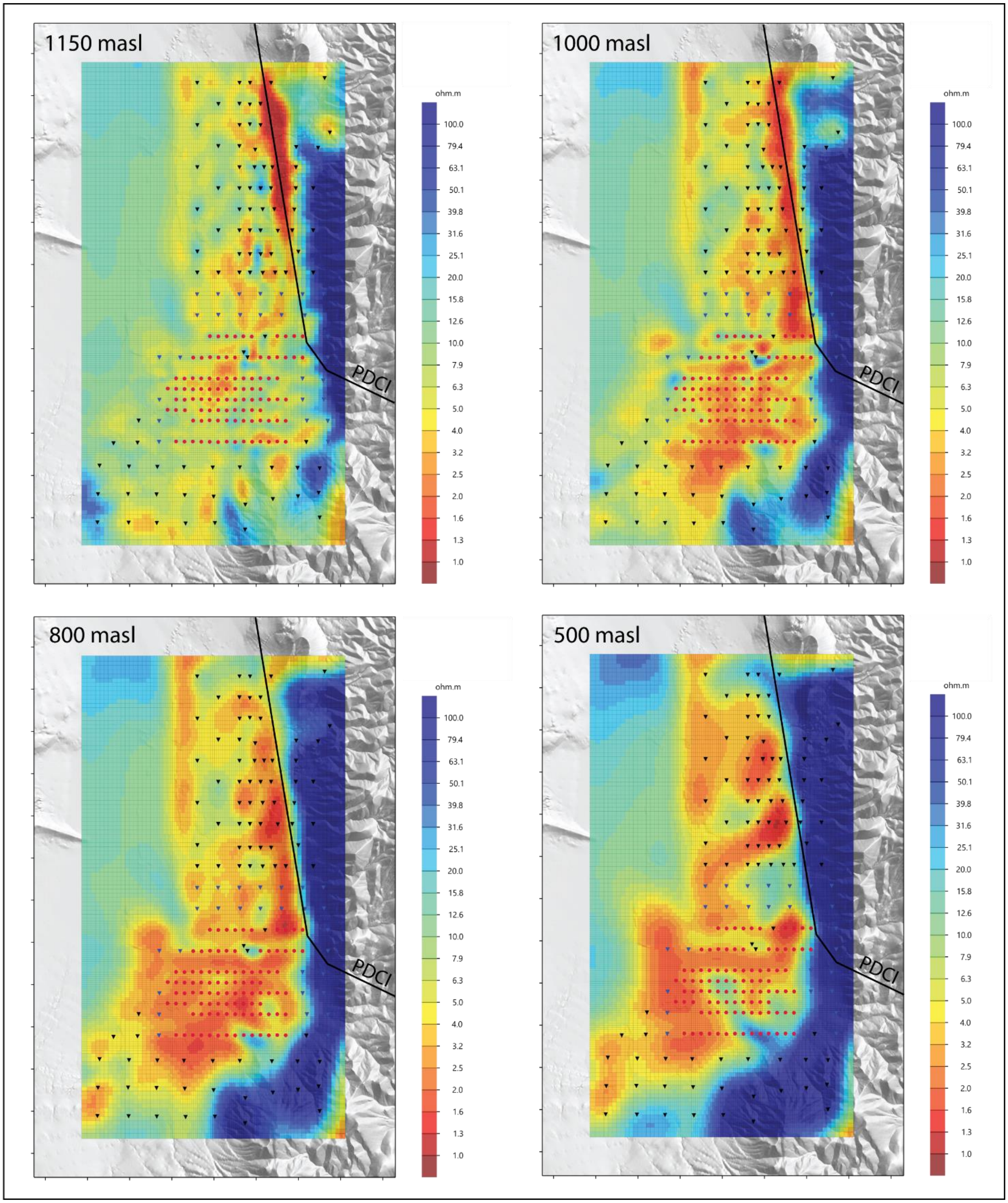

Figure 6: Constant-depth slices through the final MT inverse model. Black triangles show Zonge MT sites, blue triangles show Quantec MT sites, and red circles denote Quantec profile MT sites. PDCI is shown as a solid black line.

4.2 Gravity

4.2.1 Data Collection and Reduction

A dense gravity dataset was collected over the San Emidio geothermal system in three different phases by MWH Geo as a part of DOE cost share exploration and research grants (Figure 7A). A total of 1207 stations were collected using either Scintrex CG-5 or LaCoste and Romberg Model-G gravity meters. Elevation control was performed using real-time kinematic (RTK) GPS. Data were reduced to complete Bouguer anomaly using standard reduction equations (Telford et al., 1990) with terrain corrections handled digitally. A 10m DEM was used for terrain correction between the range of 10 m and 5 km, followed by 30 arc-second DEM for distances between 5 km 15 km. A 90-arc second DEM was used for distances up to 167 km. Digital terrain corrections accounted for earth curvature at distances greater than 15 km from each station. A reduction density of 2.3 g/cm^3 was chosen for display and modeling, which strikes a balance between low density basin fill and heavier volcanic and metamorphic rocks that outcrop in the survey area. The reduced data were gridded using a minimum curvature algorithm at 30 m grid spacing. Also shown are horizontal gradient magnitude (Figure 7B) and the gravity first vertical derivative (1VD), upward continued by 50 m (Figure 7C). The vertical derivative highlights dense near-surface features and is useful for delineating the edges of contacts.

A ground magnetic survey was conducted by Magee Geophysical in October of 2016 (Figure 7D). A total of 106 line-km was walked with Geometrics model G-858 magnetometers. Positioning was constrained by real-time differentially-corrected GPS. Data were recorded continuously at 2-second intervals. A base station was co-recorded during all periods of data acquisition to remove diurnal trends. This survey was walked at 200 m line spacing and enveloped a smaller magnetic survey that took place in 2012. As a result, some areas near the older power plant have data at 100 m line spacing. The two surveys were merged, and a reduced-to-pole transformation was applied. The data are gridded at 40 m spacing.

4.2.2 Data Characteristics and Density Study

North of the power plant and along the outflow path, evidence of the San Emidio Fault zone is abundant in the gravity data. E-W profiles through the Bouguer anomaly show a short spatial wavelength gravity-high parallel to and slightly basin-ward of the Holocene scarp. An anomalous zone in the first vertical derivative heads due north of the power plant but turns SSW below the plant. This anomaly suggests a higher-density body present near the surface. Drilling data into this zone confirm a 20 – 150 m thick sequence of intense silicification and common chalcedony-pyrite-calcite mineralization lies in the shallow surface here. We infer that this silicified zone creates a shallow density contrast within the alluvium, causing the patterns seen in the gravity field. An alternate explanation is possible with severely back-tilted fault blocks along the San Emidio Fault zone. However, drilling data that intersect the 1VD anomaly support the former interpretation.

South of the power plant, potential field data show NNE-striking features associated with the step-over fault geometry. Interestingly, significant gravity and magnetic lows occurs within the step. Two wells were drilled on the northern edge of these lows, 83-21 and OW-14. 83-21 does not get out of the basin fill with a TD of 610 m and encounters heavy lacustrine deposits and a streamer of carbonized wood at 330 m deep. OW-14 hits metamorphic basement at 844 m deep. The NNE-trending structural high seen in the gravity and magnetic data splits into two directions near the southern wells. One trend continues to the SSW and the other heads south.

Based on our interpretation of the shallow silicified zone, we chose to include this unit in gravity modeling efforts if a density contrast could be quantified. We analyzed samples of the altered zone along with other rock units in the area (Table 1). Altered rocks collected include massive grey siliceous sinter with native sulfur and secondary calcite, silicified sands and lake bed sediments with encased reed casts. The average saturated bulk density of the six altered rock samples was estimated at 2.37 g/cm^3, with porosity ranging between 12% and 21%. Local gravity modeling studies in the adjacent Smoke Creek Desert (Ponce et al., 2006; Tilden et al., 2006) used a Quaternary basin fill density of 2.02 g/cm^3 in the upper 200 m, and 2.12 g/cm^3 from 200 – 600 m depth. In either case, the measured density contrast between the alluvium and altered sediments is sufficient to explain the observed anomaly. These results are corroborated by the MT model, which shows a slightly resistive body in a conductive background just below the mapped anomaly in the gravity 1VD. We refer to this unit in this report as Qas, for silicified Quaternary alluvium. Samples were also analyzed of the older Tertiary silicified sediments near the Wind Mountain mine (units Tss an Ts in Figure 1); these units are even denser than Qas and shown in Table 1.

To estimate other rock densities, we relied upon the density lab results of Tilden et al. (2006) as well as a collection of new laboratory-derived density estimates to account for local variability (Table 2). Local samples agreed with the results of Tilden et al. rather well, except for Tertiary basalts sampled at San Emidio, which measured much denser. After compiling these data, we modeled gravity along profiles with the most well control first, to further calibrate the bulk densities of rock units. After trial and error along several profiles, we used the bulk densities shown in Table 2 for all modeled gravity profiles.

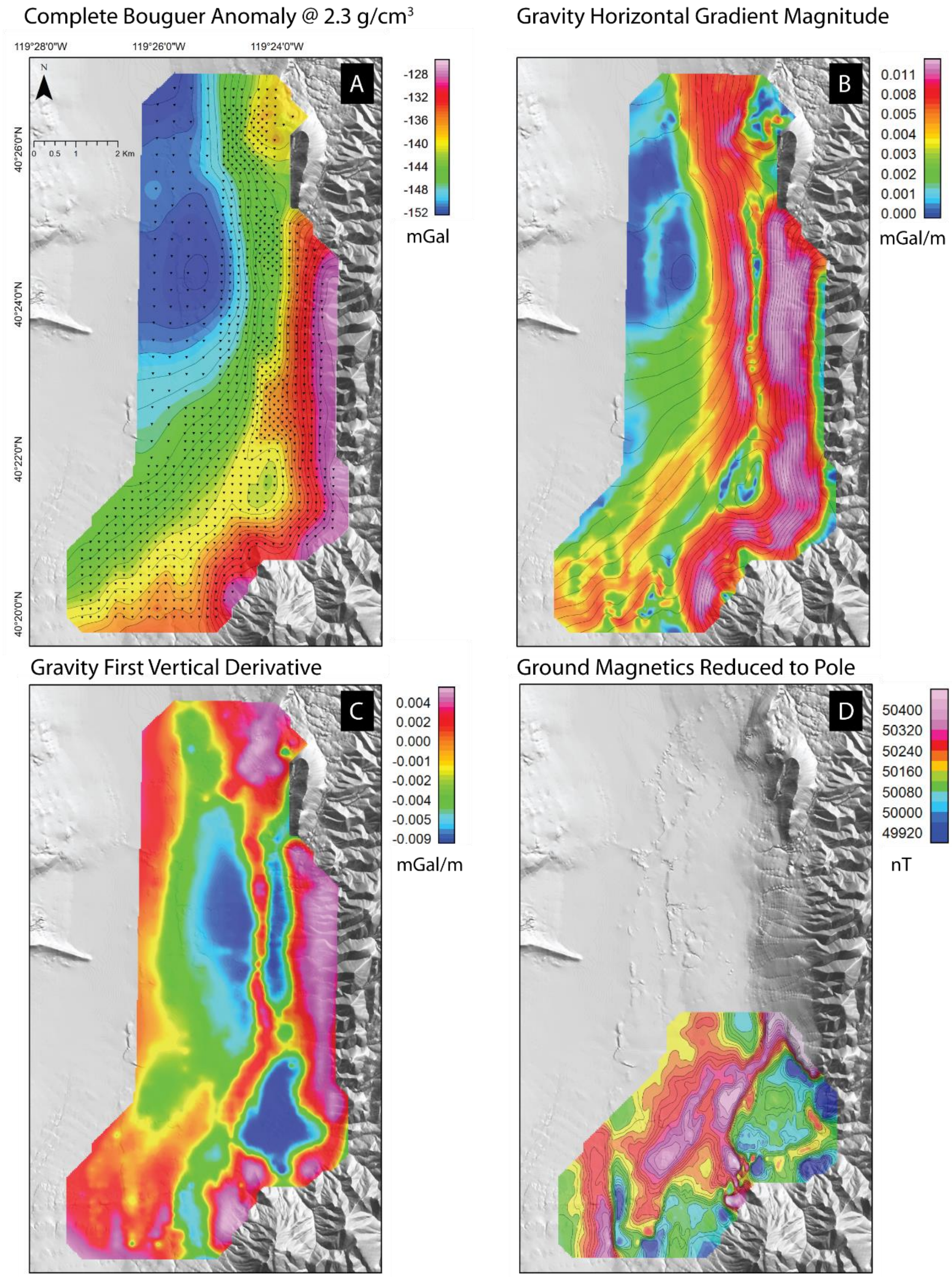

Figure 7: Potential field data collected over the study area. Top left: complete Bouguer gravity anomaly, reduced at 2.3 g/cm^3 and contoured at 1 mGal. Gravity stations are indicated by black triangles. Top right: horizontal gradient magnitude of the anomaly. Lower left: First vertical derivative of the anomaly (1VD), upward continued 50 m. Lower right: ground magnetic survey, contoured at 40 nT.

Table 1: Rock Density Data

Rock type	Abbr.	Location	Source	# of Samples	Grain Density	Dry Bulk Density	Saturated Bulk Density
Volcanics and basement							
Nightingale metamorphic (gneiss)	TrJn	Smoke Creek	Tilden et al. (2006)	2	2.72	2.62	2.66
Nightingale metamorphic (metaseds)	TrJn	Smoke Creek	Tilden et al. (2006)	7	2.65	2.43	2.52
Nightingale metamorphic (metaseds)	TrJn	Lake Range	Ormat	3	2.77	2.62	2.67
Andesite	Tvu	Smoke Creek	Tilden et al. (2006)	11	2.59	2.46	2.51
Basalt	Tpb	Smoke Creek	Tilden et al. (2006)	56	2.64	2.56	2.59
Basalt	Tpb	Lake Range	Ormat	2	3.01	2.84	2.89
Altered Silicified Sediments							
Quaternary silicified	Qas	Lake Range	Ormat	6	2.63	2.27	2.37
Tertiary silicified	Ts & Tss	Lake Range	Ormat	6	2.78	2.46	2.57

Table 2: Modeled Rock Density Values

Rock type	Abbr.	Model Density
Triassic metasediments (basement)	TrJn	2.67
Tertiary andesites and tuffaceous units	Tvu	2.6
Tertiary basalt	Tpb	2.8
Quaternary silicified sediments	Qas	2.4
Alluvial fill (0 - 200m deep)	Qal	2.02
Alluvial fill (0 - 200m deep)	Qal	2.12

4.2.3 Gravity Modeling

To model density in such a way that could include the silicified outflow zone, incorporate drilling data and match the geologic map of Rhodes et al., (2011), we chose a standard 2D forward modeling routine. Fifteen gravity profiles were modeled using the GM-SYS advanced profile modeling software, a component of Oasis Montage (Version 9.3). The program calculates a forward response using methods based on Talwani et al, (1959) and Talwani and Heirtzler (1964). Two requirements for well-constrained 2D models are that the data are relatively 2D in nature and do not have a significant regional trend (or that trend has been removed). The San Emidio gravity data meet these criteria. Figure 8A shows the 15 modeled profiles on top of Bouguer anomaly contours. The nine northern-most profiles run E-W, and the six southernmost profiles run NE-SW to best fit a bend in gravity contours there. The 2D assumptions may be less justified where this azimuth in gravity contours changes, however, we were able to construct reasonable models here. A constant DC shift of -919.981 mGals was applied to all lines after being determined by modeling profiles with the most well control.

Two sample gravity models are shown in Figure 8B. Gravity data are shown above the cross-section as black dots, with the solid line representing the forward response to the 2D model. In the northern model shown here, note the short spatial wavelength gravity high above the piedmont fault system. Here we have modeled the San Emidio fault just range-ward of the major basin-bounding fault with the largest amount of throw (>1 km). The silicified zone, Qas, is modeled as in imbedded dense body above it. This profile is constrained by wells 75B-16 and 76-16, which sample the silicified zone and constrain the depth to the volcanic layers. Each gravity model was constructed using the MT volume as a backdrop, to guide depth to basement in the absence of well data and delineate the location of the silicified zone, which appears as a subtle resistor in most cross sections. The southern exploration wells encounter less distinct, and much thinner layers of silicified alluvium. Instead they pass through thick layers of intense clay alteration (~300 m in well 18-21).

Profiles through the southern wellfield pass over the distinct gravity and magnetic low tucked within the step-over. Modeling gravity here requires a distinct deficit of mass to match the data, and current drilling data does inform the structure here. We modeled this mass deficit as a small graben structure bound by an NNE-striking, east-dipping antithetic fault. Although we did not model magnetic data in this project, we infer that the distinct magnetic low denotes an absence of magnetized rocks here. One explanation for the absence of magnetic rocks is that the alluvial contact here is with meta-sediments, which are more likely to have low susceptibilities and remnant magnetism, as shown locally by Tilden et al. (2006). It is possible that volcanic units did not accumulate here due to the paleo-topography, or they were removed via erosion during rifting.

Horizons for the different rock units were extracted from the gravity models and used to create a 3D block model in Leapfrog Geothermal software. This program allows for fault surfaces and lithologic horizons to be controlled by editing meshes, enforcing fault interactions such as crossings or terminations, and by controlling lithologic relationships. These tools allow for connecting the different gravity models in a geologically-sensible manner, while being mindful of other datasets draped on topography or in 3D space, such as the 3D MT volume. The final block volume is constructed from five lithologies (TrJn, Tvu, Tpb, Qas and Qal), 12 fault zones and has 17 total fault blocks. A slice through the block model with basin-fill removed is shown in Figure 8C. Horizons to the base of alluvium from each model are shown as yellow lines. Figure 8A shows the projected surface trace of the modeled faults (Green lines). We have modeled San Emidio Fault zone (red line) as arcuate shaped, rather than by separate linear connected segments as earlier interpretations by Matlick (1995). However, we acknowledge that the faults can be connected in different ways and this is only our interpretation. Additionally, this modeling strategy is insensitive to E-W trending structures, if present.

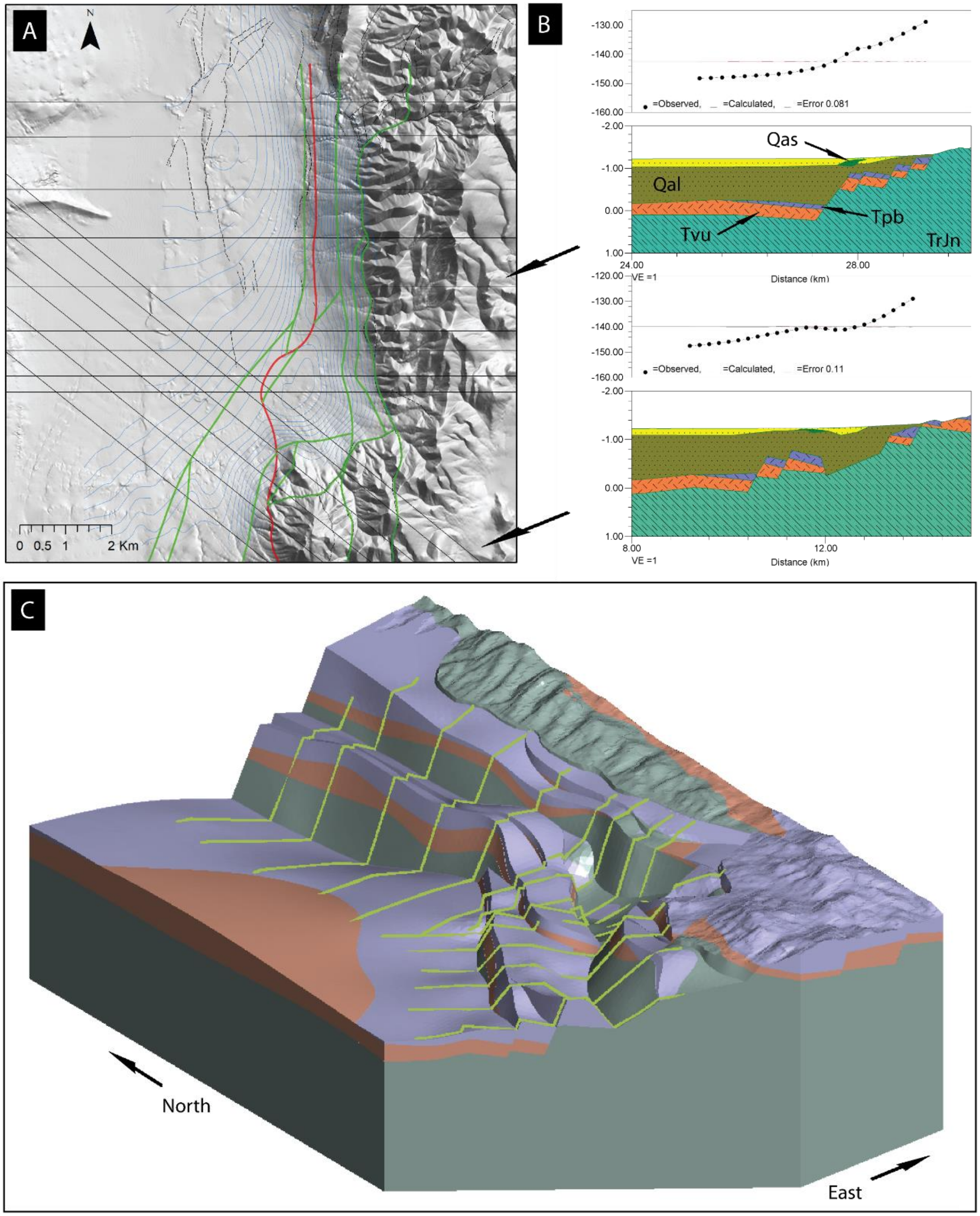

Figure 8: (A) Map showing 15 profiles along which gravity was modeled. Gravity contours are in light blue. Green lines denote where modeled faults intersect the ground surface. The modeled San Emidio fault zone is shown in red. Thin black lines denote faults from Rhodes et al, (2010) (B) Sample gravity models. Data along each profile is shown as black dots. Model fit is shown as a thin black line. Geologic units denoted by color-filled section. (C) Conceptual geologic block model constructed from the gravity models, with basin fill units removed. Yellow lines show horizons extracted from each model that denote the base of the alluvium.

5. RESULTS

5.1 MT and Geologic Modeling

Figure 9 shows four E-W slices though the final modeled volumes, from north to south. In each frame, the geologic model is shown in the upper image, with the gravity 1VD draped over topography. The MT model is shown in the lower panel of each image, with the MT station locations draped on topography. Modeled faults are shown as black lines. Each slice shows the silicified unit Qas as a blue outline, though it is not modeled in the southern-most slice (Figure 9 D) and is believed to thin and terminate near well 18-21.

The northern-most section (Figure 9A) slices through the outflow path, north of any production wells. A clear resistive lens lies below the gravity 1VD anomaly. The basin is the deepest on this northern line, with approximately 1.5 km of throw on the most westward modeled fault. The MT model also suggests the basin is at its deepest here. This deep portrayal differs from Rhodes (2011) but is required to fit the data. This geometry is also supported by the work of Basler-Reeder (2015), who used the same gravity data along with 2D seismic refraction and reflection data collected here in 2010. This joint optimization project using gravity and seismic data concluded that the valley floor was at least 1.5 km deep.

Figure 9B shows the model sliced through well 75-16, near the current power plant and over the northernmost expression of a deep, fault hosted reservoir. Silicified unit Qas is again modeled on a resistive lens in a conductive background, and under the gravity 1VD anomaly. A feed zone in well 75-16 sources from the reservoir and strikes the San Emidio fault zone under a dome-shaped conductor near the 6-8 ohm-m contours in the MT model. The dome geometry appears partially breached by a resistive column, and the conductor is the strongest (<1.5 ohm-m) east of the dome where it is bound between two normal faults. A deep conductor in the basin is poorly constrained with no MT stations above it.

Figure 9C slices through southern exploration well 18-21, where the highest temperatures yet discovered are located under a thick sequence of heavy clay alteration. This profile crosses a NNE-trending basement high and fault structure. The shallow silicified zone is thinner and less distinct in well data here and does not correlate as well with resistivity. Well 18-21 sources from heavily fractured volcanic rock, which we have also modeled as the San Emidio fault zone. Again, feed zones occur near the 6 – 8 ohm-m contours, under a well-formed conductive dome. This profile passes through the deepest part of the gravity low within the step-over, and over the antithetic (east-dipping) fault. The MT model supports a back-basin here, but with a unexplained second dome that is not evident in other datasets.

The southernmost profile (Figure 9D) passes through the southern step-over structure. Not at all constrained by drill data, the model here is informed only by surface geology and geophysical data. Previous mapping (Rhodes, 2011) show that this area is rich with fault complexity, and our modeling efforts support this conclusion. We interpret the gently-dipping basin-contact conductor as apparent dip from more E-W trending fault segments. The major dome-shaped conductor in Figure 9C is ridge-shaped in 3D, and continues to the SSE, where it shallows and meets up with the distinct resistive break in the conductor in Figure 9D.

Much attention has been given to the geometry of resistivity anomalies over geothermal systems (Ucok et al., 1980; Ussher et al., 2000, Cumming, 2009, Cumming and Mackie, 2010). Collectively these studies attribute dome-shaped conductors over geothermal systems to temperature-dependent argillic alteration of varying conductivities. Here we observe that intense clay alteration does drape over these reservoirs, but that the buried-horst geometry also plays a role in these patterns, especially in the southern portion of the field.

Figure 10 shows a conceptual model of the San Emidio geothermal system drawn parallel to the outflow path. A fence section begins near southern wells 18-21 and 78-20 and slices towards the current power plant location. From there it turns due north and along the ~5 km long outflow path. We infer that deep, ~165°C fluids rise along dilatant zones within NNE striking, accommodating faults of the relay structure. These fluids are conveyed to the NNE by fault structures and rise near the power plant where they heavily precipitate silica and other reducing mineral assemblages. Here outflow enters a second, shallow reservoir hosted by fractured and silicified sedimentary units, and bound by piedmont faults where it becomes channelized to the north and eventually entrained with shallow groundwater. Along this path the zone of advanced argillic alteration continues for some distance. The current southern margin of the commercial field remains unconstrained by drilling data.

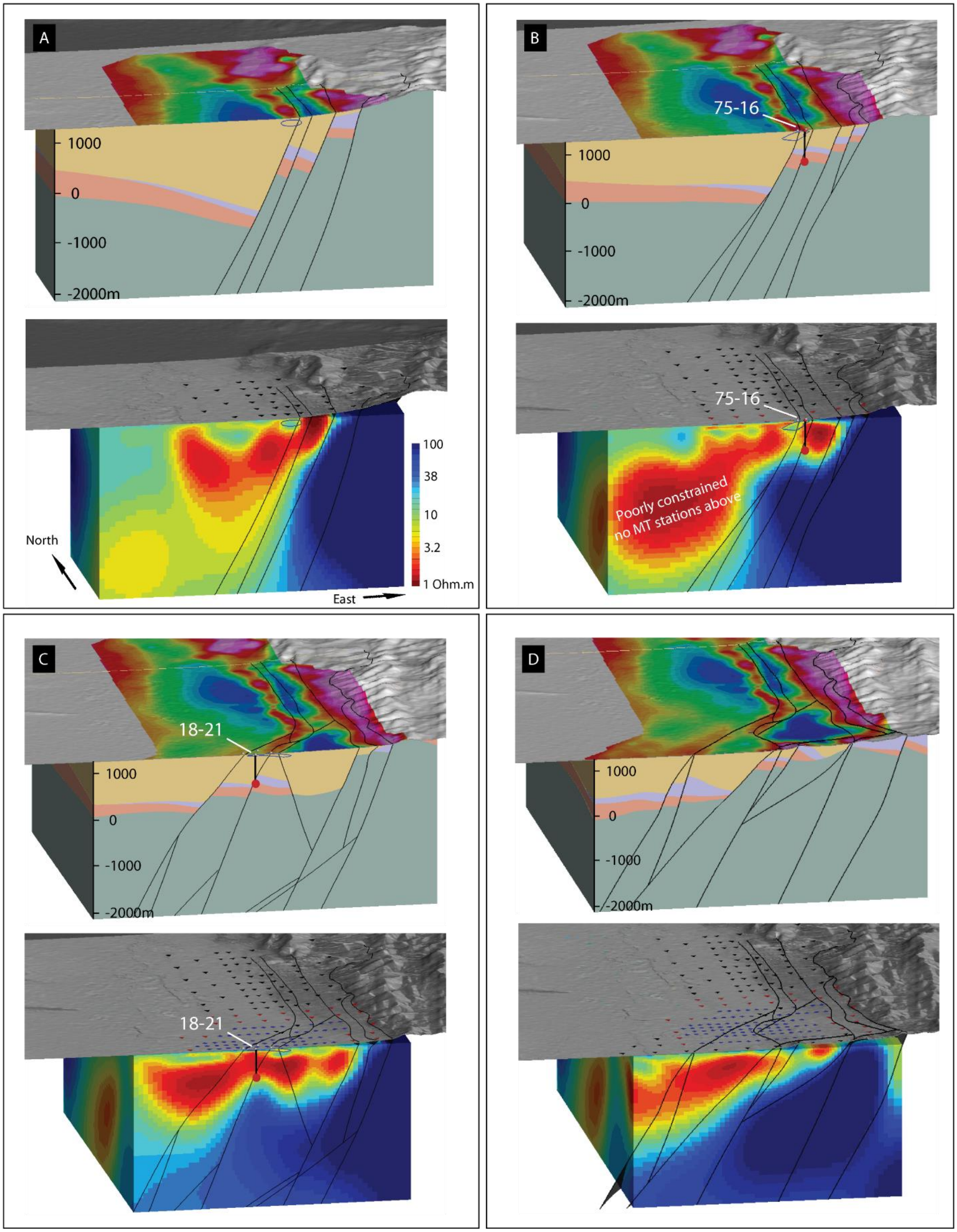

Figure 9: (A-D) Slices through the conceptual block model, from north to south. The upper view of each panel has the gravity 1VD draped over topography and the geologic model in cross-section. The lower view in each panel has the MT station locations draped over topography, and the 3D MT model in cross-section. Modeled faults are shown as black lines. Blue ellipses denote altered alluvium (Qas) along outflow (A-C only). Two wells are shown with feed zone locations as red dots.

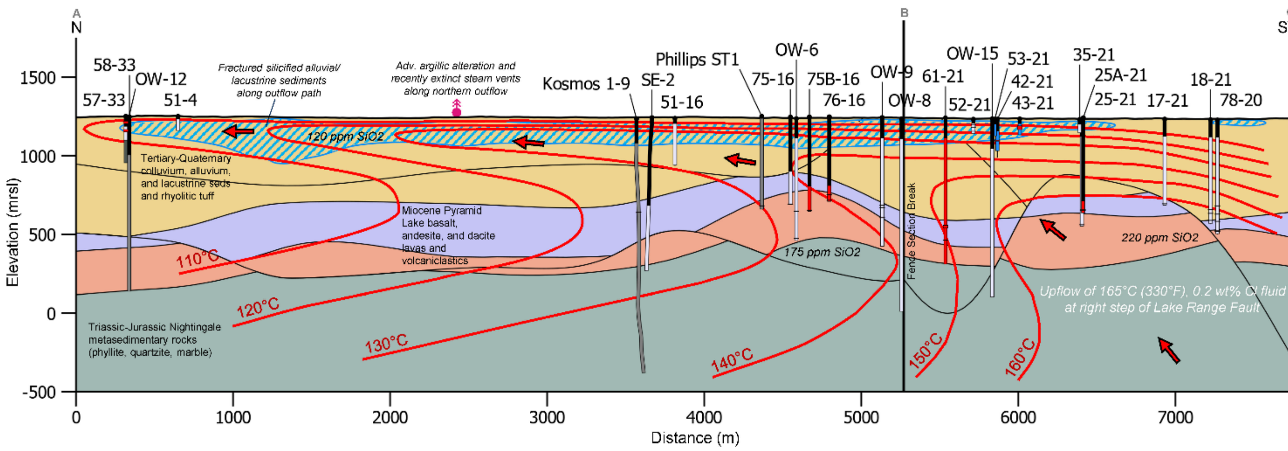

Figure 10: (A) Conceptual geologic model sliced along a fence section connecting wells in across the field. Red lines show isotherms of pre-development temperatures, indicating deep upflow in the southern portion of the field, and shallow outflow to the north along the San Emidio fault zone. Heavy silicified sediments are shown as a blue cross-hatched outline.

5.2 Comparison of Results with Passive Seismic Emission Tomography

In 2016 an experiment to map subsurface permeability was conducted over the southern portion of the San Emidio field. The project was part of a DOE cost share grant (DE-EE0007698) and included collection of a large passive seismic dataset and the Quantec MT data presented in this report (Warren et al., 2018). Microseismic Inc. (MSI) collected seismic data for two related experiments: (1) A traditional passive seismic emission tomography (PSET) experiment designed to identify discrete events using a short, 100 ms time window; and (2) A closely related technique using a longer, 1-hour time window designed to map zones of elevated acoustic energy. This later technique is referred to by MSI as rPSET, though other practitioners have called it Tomographic Fracture Imaging™, or TFI (Geiser et al, 2006, 2012; Lacazette and Geiser, 2013; Sicking et al., 2013). The later of these experiments was among the first to be applied to a geothermal field; previous applications have traditionally monitored hydraulic fracturing treatments, and more recently, mapped natural fracture zones that may be favorably stimulated by hydraulic fracturing (Lacazette et al, 2013). Here we compare the results of the rPSET experiment with our geophysical and geologic models

The rPSET method employs a dense, gridded, multi-component array of geophones to passively listen, ideally, while no man-made sources of noise are present. A study area in 3D is divided into a voxel, and, using a beam-forming technique, a measure of relative acoustic energy such as semblance is assigned to each location. Many such voxels are generated for different time windows, and then stacked to remove noise. The final data product is a voxel that illuminates areas of greater seismic emission energy. In the case of the San Emidio experiment, the velocity model used was constructed from a novel machine-learning algorithm (Warren et al., 2018), though the unconventional oil and gas industry uses other methods. The long-time window precludes the ability to discern relative magnitude or focal mechanisms from events and cannot locate single events well at all. Rather, the technique locates very small repetitive events.

The method is relevant to geothermal for a few important reasons, as summarized nicely by Lacazette et al. (2013). The primary reason being that the amount of shear stress on fractures correlates positively to the hydraulic transmissivity on those fractures (Barton et al, 1995; Heffer et al, 1995; Morris et al, 1996; Sibson 2000; Ito and Hayashi, 2003 and many others). Elevated shear stress also correlates with micro-seismicity.

Visualizing the final voxel in useful ways can be challenging. Warren et al. (2018) chose to sum the semblance values vertically in each column of the voxel to create a map-view reorientation of acoustic energy (reproduced here in Figure 11A). This vertical stacking further reduces random noise. This portrayal demonstrated a correlation between elevated acoustic energy and drilling success in the southern field near well 18-21. Here we also show the data in cross-section next to the 3D MT volume. To eliminate noise in the rPSET cross-section, we gridded a slice through the voxel using a least-squares grid fit. The original voxel has a data point approximately every 30m. We gridded slices though the voxel at 10m mesh spacing and included points off the line using a 90 m bandwidth. In this way the data are 'stacked' perpendicular to the profile. A slice through the voxel and through well 18-21 are shown n Figure 11C. MT data are shown in Figure 11B. 1302 stations each with 6 geophone locations are shown as grey triangles in Figure 11A.

The results show an elevated zone of acoustic energy located near the modelled San Emidio fault zone, feed zones in well 18-21 and directly under a dome-shaped conductor in the MT volume. Most of the energy appears to be hosted in the tertiary volcanic units and the basement below.

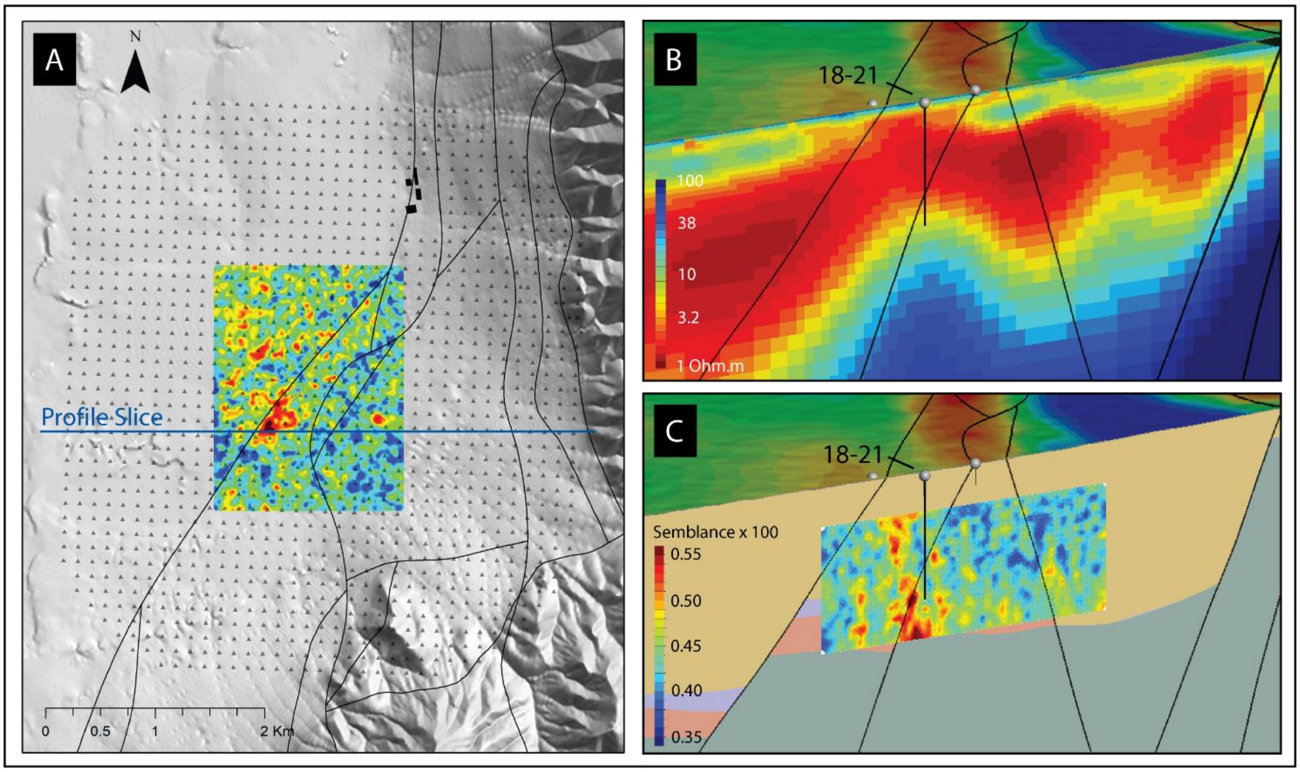

Figure 11: (A) Map showing geophone locations (gray triangles) and vertically-summed semblance scores from the PSET volume. Modeled faults are in shown as black lines. Power plant buildings are shown as black polygons. (B) Slice through the MT volume and through well 18-21. (C) The same slice through the geologic model and PSET volume.

6. DISCUSSION

As this study progressed, it became clear that two salient aspects of the San Emidio field deserve special notice. The first is the unique characteristics of the outflow path, and how it might inform the development of future blind systems; the second is recognizing that the step-over geometry was key to maximizing this resources' potential.

The zone of shallow outflow here is a unique given its geometry and physical attributes. The zone hosts a short spatial wavelength gravity high and 1VD anomaly, a tube-like resistive lens that lies beneath the surface, and was found to subside at a rate of near 2 mm/yr using PinSAR during the period 2003 – 2010 due to production (Eneva et al, 2011; Teplow and Warren 2015, Reinisch et al., 2019). Early efforts to model the gravity here that accounted only for the basement contact fit the data poorly along this zone (Teplow and Warren 2015). Generation of a shallow, densified, yet relatively porous silicified zone seems like a plausible explanation and is supported by hydrothermal mineralization documented in wells that intersect this zone. Gravity highs attributed to densification of sediments at geothermal sites in the Imperial Valley have been described by Biehler (1971), but densification along outflow paths is not well documented. A similar geometry in the gravity is observed at the Brady's geothermal system (Folsom et al., 2018), and a prominent gravity 1VD anomaly delineates near-surface alteration at Ormat's Don A. Campbell field in NV (unpublished report). Many other sites have no such gravity signature, however. Clearly, this area of study deserves more attention.

Upon projecting the modeled faults in the southern portion of the field to the surface, it becomes apparent that the fault geometry bears a striking similarity to the step-over structure located to the north at the Wind Mountain mine. One possible implication is that the northern stepover is responsible for the location of the extinct geothermal system and is therefore an analogy for the current system to the south. At the northern stepover (Figure 1), where the range front normal fault terminates into a ENE-striking oblique fault as mapped by Rhodes (2010), it also splinters to the north where it meets with a NNE-striking, west-dipping normal fault. This intersection is at the location of one of the mine pits that hosted the greatest mineralization. At the southern step-over, the pattern is repeated. The range front fault takes a hard-right turn, but geophysical data show that a strand splinters northward, where it meets with NNE-striking structure. That intersection lies below well 18-21 and the inferred center of the deep reservoir.

6. CONCLUSIONS

The San Emidio geothermal system has a set of unique geophysical characteristics that make it a useful and relevant case study. The system is hosted by dilatant, accommodating structures associated with a right step in normal faulting. The reservoir has been imaged such that it is overlain by thick (~300 m or more) sequences of advanced argillic alteration of sediments, along a NNE-striking basement high with characteristics of a buried, faulted horst block. Structural elements within the reservoir remain under significant shear stress as suggested by enhanced semblance of passive seismic signals. This zone is found to be co-located with doming in the conductive clay cap. The geometry of the relay ramp structure, somewhat resolved here via collaborative modeling, bears a striking similarity to another right step in the Lake Range ~7 km to the north, that hosts a Miocene hot-spring style, epithermal gold and silver deposit. Perhaps most striking about the San Emidio system is a long, range-parallel, linear zone of silicified sediments and acid-sulfate mineralization that reflects a prominent and channelized outflow path. This zone is found to have an elevated density over the surrounding basin fill which creates a distinct anomaly best seen in the first vertical derivative of the gravity data. Such features, imaged elsewhere, may hint at the presence of blind or semi-hidden geothermal systems.

ACKNOWLEDGEMENTS

We'd like to thank Charlie Stevens, Andrew Hill and Michael Grealy at Microseismic for help understanding and interpreting the PSET results, which are very new to us. We'd like to thank Bill Doerner, Chet Lide, Marco Zamudio and Kam Moezzi at Zonge International for their help collecting and advising on the MT survey shown in this report. Also, thanks to Josh Sellers, Tom Popowski and Bastien Poux at Seequent for help and advice modeling the gravity data in Geosoft and building the 3D block model in Leap Frog Geothermal. This project would not have been possible without their contributions.

REFERENCES

Barton, C. A., Zoback, M. D., & Moos, D. (1995). Fluid flow along potentially active faults in crystalline rock. *Geology*, *23*(8), 683-686.

Basler-Reeder, K. J. (2015). Joint Optimization of Vertical Component Gravity and Seismic P-wave First Arrivals by Simulated Annealing (Doctoral dissertation).

Biehler, S. (1971). Gravity studies in the Imperial Valley. *Cooperative Geological-Geophysical-Geochemical Investigations of Geothermal Resources in the Imperial Valley of California: Riverside, California, University of California–Riverside Education Research Service*, 29-41.

Bonham, H. F., & Papke, K. G. (1969). Geology and mineral deposits of Washoe and Storey Counties, Nevada (Vol. 70). Mackay School of Mines, University of Nevada.

Cagniard, L. (1953). Basic theory of the magneto-telluric method of geophysical prospecting. *Geophysics*, *18*(3), 605-635.

Cox, S. F. (2005). Coupling between deformation, fluid pressures, and fluid flow in ore-producing hydrothermal systems at depth in the crust. *Economic Geology*, *100*, 39-75.

Cumming, W. (2009, February). Geothermal resource conceptual models using surface exploration data. In *Proceedings*.

Cumming, W., & Mackie, R. (2010, April). Resistivity imaging of geothermal resources using 1D, 2D and 3D MT inversion and TDEM static shift correction illustrated by a Glass Mountain case history. In *Proceedings world geothermal congress* (pp. 25-29). Indonesia: Bali.

Drakos, P. S. (2007). Tertiary stratigraphy and structure of the southern Lake Range northwest Nevada: Assessment of kinematic links between strike-slip and normal faults in the northern Walker Lane (Doctoral dissertation, University of Nevada, Reno).

Dierkhising, J. O. (2015). Development and Application of AVO Methods and Seismic Attribute Analysis for Characterization of the San Emidio Geothermal Reservoir, Northwestern Nevada (Doctoral dissertation).

Eneva, M., Falorni, G., Teplow, W., Morgan, J., Rhodes, G., & Adams, D. (2011). Surface deformation at the San Emidio geothermal field, Nevada, from satellite radar interferometry. *Geothermal Resources Council Transactions*, *35*, 1647-1653.

Faulds, J. E., Henry, C. D., & Hinz, N. H. (2005). Kinematics of the northern Walker Lane: An incipient transform fault along the Pacific–North American plate boundary. *Geology*, *33*(6), 505-508.

Faulds, J. E., Coolbaugh, M. F., Vice, G. S., & Edwards, M. L. (2006). Characterizing structural controls of geothermal fields in the northwestern Great Basin: A progress report. *Geothermal Resources Council Transactions*, *30*, 69-76.

Faulds, J. E., Hinz, N. H., Coolbaugh, M. F., Cashman, P. H., Kratt, C., Dering, G., ... & McLachlan, H. (2011). Assessment of favorable structural settings of geothermal systems in the Great Basin, western USA. *Geothermal Resources Council Transactions*, *35*, 777-783.

Faulds, J. E., Hinz, N. H., Dering, G. M., & Siler, D. L. (2013). The hybrid model—the most accommodating structural setting for geothermal power generation in the Great Basin, western USA. *Geothermal Resources Council Transactions*, *37*, 3-10.

Folsom, M., Lopeman, J., Perkin, D., & Sophy, M. (2018). Imaging Shallow Outflow Alteration to Locate Productive Faults in Ormat's Brady's and Desert Peak Fields Using CSAMT. In *Proceedings of the 43rd Workshop on Geothermal Reservoir Engineering, Stanford, CA, USA* (pp. 12-14).

Fossen, H., & Rotevatn, A. (2016). Fault linkage and relay structures in extensional settings—A review. *Earth-Science Reviews*, *154*, 14-28.

Geiser, P., Vermilye, J., Scammell, R., & Roecker, S. (2006). Seismic used to directly map reservoir permeability fields. *Oil & gas journal*, *104*(46), 37-37.

Geiser, P., Lacazette, A., & Vermilye, J. (2012). Beyond 'dots in a box': An empirical view of reservoir permeability with tomographic fracture imaging. *First Break*, *30*(7), 63-69.

Hammond, W. C., & Thatcher, W. (2005). Northwest Basin and Range tectonic deformation observed with the Global Positioning System, 1999–2003. *Journal of Geophysical Research: Solid Earth*, *110*(B10).

Heffer, K. J., Fox, R. J., McGill, C. A., & Koutsabeloulis, N. C. (1997). Novel techniques show links between reservoir flow directionality, earth stress, fault structure and geomechanical changes in mature waterfloods. *SPE Journal*, *2*(02), 91-98.

Ito, T., & Hayashi, K. (2003). Role of stress-controlled flow pathways in HDR geothermal reservoirs. *Pure and applied geophysics*, *160*(5-6), 1103-1124.

Jiracek, G. R. (1990). Near-surface and topographic distortions in electromagnetic induction. *Surveys in Geophysics*, *11*(2-3), 163-203.

Lacazette, A., Vermilye, J., Fereja, S., & Sicking, C. (2013). Ambient fracture imaging: a new passive seismic method. *Unconventional Resources Technology Conference (URTEC).*

Mackie, R. L., Rodi, W., & Watts, M. D. (2001). 3-D magnetotelluric inversion for resource exploration. In *SEG Technical Program Expanded Abstracts 2001* (pp. 1501-1504). Society of Exploration Geophysicists.

Mackie, R. L., & Madden, T. R. (1993). Three-dimensional magnetotelluric inversion using conjugate gradients. *Geophysical Journal International*, *115*(1), 215-229.

Matlick, S., (1995). San Emidio Geothermal System, Empire, NV. *GRC Field Trip – October 1995*. Mesquite Group, Inc.

Moore, J. N. (1979). Geology map of the San Emidio, Nevada geothermal area (No. DOE/ET/28392-33). Utah Univ., Salt Lake City (USA). Earth Science Lab.

Morris, A., Ferrill, D. A., & Henderson, D. B. (1996). Slip-tendency analysis and fault reactivation. *Geology*, *24*(3), 275-278.

Ponce, D. A., Glen, J. M., & Tilden, J. E. (2006). Geophysical investigations of the Smoke Creek Desert and their geologic implications, northwest Nevada and northeast California. US Geological Survey.

Reinisch, E. C., Cardiff, M., Akerley, J., Warren, I., & Feigl, K. L. (2019). Spatio−Temporal Analysis of Deformation at San Emidio Geothermal Field, Nevada, USA Between 1992 and 2010. *Remote Sensing*, *11*(16), 1935.

Rhodes, G. T., Faulds, J. E., Teplow, W. (2010). Structural Controls of the San Emidio Geothermal Field, Northwestern Nevada. *GRC Transactions,* Vol. 34.

Rhodes, G. T., Faulds, J. E., Ramelli, A. R. (2011). Preliminary Geologic Map of the Northern Lake Range, San Emidio Geothermal Area, Washoe County, Nevada. Nevada Bureau of Mines and Geology, Open-File report, 11-11.

Rhodes, G. T. (2011). Structural Controls of the San Emidio Geothermal System, Northwestern Nevada. University of Nevada, Reno.

Ristorcelli, S., Dyer., T. L., (2012) Updated Technical Report and Preliminary Economic Assessment Wind Mountain Gold-Silver Project Washoe County, NV. Prepared for Bravada Gold Corporation. Mine Development Associates, Reno NV.

Rodi, W. and Mackie, R.L. (2001). Nonlinear conjugate gradients algorithm for 2D magnetotelluric inversion. *Geophysics, 66, 174-187*

Sibson, R. H. (2000). Fluid involvement in normal faulting. *Journal of Geodynamics*, *29*(3-5), 469-499.

Sicking, C., Vermilye, J., Geiser, P., Lacazette, A., & Thompson, L. (2012). Permeability field imaging from microseismic. In *SEG Technical Program Expanded Abstracts 2012* (pp. 1-5). Society of Exploration Geophysicists.

Soyer, W., Hallinan, S., Mackie, R. L., & Cumming, W. (2008, June). Statics in magnetotellurics-shift or model? In *70th EAGE Conference and Exhibition incorporating SPE EUROPEC 2008* (pp. cp-40). European Association of Geoscientists & Engineers.

Soyer, W., Mackie, R., & Miorelli, F. (2018a). Optimizing the Estimation of Distortion Parameters in Magnetotelluric 3D Inversion. In *80th EAGE Conference and Exhibition 2018* (Vol. 2018, No. 1, pp. 1-5). European Association of Geoscientists & Engineers.

Soyer, W., Mackie, R.L., Hallinan, S., Pavesi, A., Nordquist, G., Suminar, A., Intani, R. and Nelson, C. (2018b). Geologically-consistent multiphysics imaging of the Darajat geothermal steam field. *First Break*, 36(6), 77-83.

Talwani, M., Worzel, J. L., & Landisman, M. (1959). Rapid gravity computations for two-dimensional bodies with application to the Mendocino submarine fracture zone. *Journal of geophysical research*, *64*(1), 49-59.

Talwani, M., & Heirtzler, J. R. (1964). Computers in the Mineral Industries, Part 1.

Teplow William, James Faulds, Greg Rhodes, Inga Moeck, Mariana Eneva, Satish Pullamannapallil, (2011), Finding Large Aperture Fractures in Geothermal Resource Areas Using a Three-Component Long-Offset Surface Seismic Survey, PSInSAR and Kinematic Structural Analysis, DOE Award No.: DE-EE0002847, Phase 1 Final Report, September 12, 2011.

Teplow, W. J., & Warren, I. (2015). Finding Large Aperture Fractures in Geothermal Resource Areas Using a Three-Component Long-Offset Surface Seismic Survey, PSInSAR and Kinematic Structural Analysis (No. DOE-US Geothermal Inc-0002847). US Geothermal, Inc., Boise, ID (United States).

Tilden, J. E., Ponce, D. A., Glen, J. M., Chuchel, B. A., Tushman, K., & Duvall, A. (2006). Gravity, magnetic, and physical property data in the Smoke Creek Desert area, northwest Nevada (No. 2006-1197).

Tikhonov, A.N. and Arsenin, V.Y. (1977). Solutions of ill-posed problems, *V. H. Winston and Sons.*

Ucok, H., Ershaghi, I., & Olhoeft, G. R. (1980). Electrical resistivity of geothermal brines. *Journal of Petroleum Technology*, *32*(04), 717-727.

Ussher, G., Harvey, C., Johnstone, R., & Anderson, E. (2000, May). Understanding the resistivities observed in geothermal systems. In *proceedings world geothermal congress* (pp. 1915-1920). Kyushu.

Warren, I., Gasperikova, E., Pullammanappallil, S., & Grealy, M. (2018, February). Mapping geothermal permeability using passive seismic emission tomography constrained by cooperative inversion of active seismic and electromagnetic data. In *Proceedings of the 43rd Stanford Workshop on Geothermal Reservoir Engineering, Stanford, CA, USA* (pp. 12-14).